First clinical assessment of [18 F]MC225, a novel fluorine-18 labelled PET tracer for measuring functional P-glycoprotein at the blood-brain barrier

Toyohara, Jun; Sakata, Muneyuki; Ishibashi, Kenji; Mossel, Pascalle; Imai, Masamichi; Wagatsuma, Kei; Tago, Tetsuro; Imabayashi, Etsuko ; Colabufo, Nicola Antonio; Luurtsema, Gert

Published in:
ANNALS OF NUCLEAR MEDICINE

DOI:
10.1007/s12149-021-01666-9

Publication date:
2021

Annals of Nuclear Medicine (2021) 35:1240–1252
https://doi.org/10.1007/s12149-021-01666-9

ORIGINAL ARTICLE

First clinical assessment of [^{18}F]MC225, a novel fluorine-18 labelled PET tracer for measuring functional P-glycoprotein at the blood–brain barrier

Jun Toyohara[1] · Muneyuki Sakata[1] · Kenji Ishibashi[1] · Pascalle Mossel[2] · Masamichi Imai[1] · Kei Wagatsuma[1,3] · Tetsuro Tago[1] · Etsuko Imabayashi[4] · Nicola A. Colabufo[5] · Gert Luurtsema[2] · Kenji Ishii[1]

Received: 25 May 2021 / Accepted: 2 August 2021 / Published online: 8 August 2021

Abstract

Objective 5-(1-(2-[^{18}F]fluoroethoxy))-[3-(6,7-dimethoxy-3,4-dihydro-1H-isoquinolin-2-yl)-propyl]-5,6,7,8-tetrahydronaphthalen ([^{18}F]MC225) is a selective substrate for P-glycoprotein (P-gp), possessing suitable properties for measuring overexpression of P-gp in the brain. This is the first-in-human study to examine safety, radiation dosimetry and P-gp function at the blood–brain barrier (BBB) of [^{18}F]MC225 in healthy subjects.

Methods [^{18}F]MC225 biodistribution and dosimetry were determined in 3 healthy male subjects, using serial 2 h and intermittent 4 and 6 h whole-body PET scans acquired after [^{18}F]MC225 injection. Dynamic [^{18}F]MC225 brain PET (90 min) was obtained in 5 healthy male subjects. Arterial blood was sampled at various time intervals during scanning and the fraction of unchanged [^{18}F]MC225 in plasma was determined. T1-weighted MRI was performed for anatomical coregistration. Total distribution volume (V_T) was estimated using 1- and 2-tissue-compartment models (1-TCM and 2-TCM, respectively). V_T was also estimated using the Logan graphical method (Logan plot) ($t^* = 20$ min). Surrogate parameters without blood sampling (area-under the curve [AUC] of regional time–activity curves [TACs] and negative slope of calculated TACs) were compared with the V_T values.

Results No serious adverse events occurred throughout the study period. Although biodistribution implied hepatobiliary excretion, secretion of radioactivity from liver to small intestine through the gallbladder was very slow. Total renal excreted radioactivity recovered during 6 h after injection was < 2%ID. Absorbed dose was the highest in the pancreas (mean ± SD, 203 ± 45 μGy/MBq) followed by the liver (83 ± 11 μGy/MBq). Mean effective dose with and without urination was 17 ± 1 μSv/MBq. [^{18}F]MC225 readily entered the brain, distributing homogeneously in grey matter regions. 2-TCM provided lower Akaike information criterion scores than did 1-TCM. V_T estimated by Logan plot was well correlated with that of 2-TCM ($r^2 > 0.9$). AUCs of TACs were positively correlated with V_T (2-TCM) values (r^2: $AUC_{0\text{-}60\ min} = 0.61$, $AUC_{0\text{-}30\ min} = 0.62$, $AUC_{30\text{-}60\ min} = 0.59$, $p < 0.0001$). Negative slope of SUV TACs was negatively correlated with V_T (2-TCM) values ($r^2 = 0.53$, $p < 0.0001$).

Conclusions This initial evaluation indicated that [^{18}F]MC225 is a suitable and safe PET tracer for measuring P-gp function at the BBB.

Keywords P-glycoprotein · Blood–Brain barrier · Positron emission tomography · Dosimetry · First-in-human

✉ Jun Toyohara
toyohara@pet.tmig.or.jp

[1] Research Team for Neuroimaging, Tokyo Metropolitan Institute of Gerontology, 35-2 Sakae-cho, Itabashi-ku, Tokyo 173-0015, Japan

[2] Department of Nuclear Medicine and Molecular Imaging, University of Groningen, University Medical Center Groningen, Hanzeplein 1, 9713 GZ Groningen, The Netherlands

[3] School of Allied Health Science, Kitasato University, 1-15-1 Kitasato, Sagamihara, Kanagawa 252-0373, Japan

[4] Department of Diagnostic Radiology, Tokyo Metropolitan Geriatric Hospital and Institute of Gerontology, 35-2 Sakae-cho, Itabashi-ku, Tokyo 173-0015, Japan

[5] Dipartimento di Farmacia-Scienze del Farmaco, Università degli Studi di Bari, via Orabona 4, 70125 Bari, Italy

Introduction

The blood–brain barrier (BBB) plays an important role in protecting the brain from xenobiotics and in maintaining homeostasis in the internal environment of the central nervous system [1]. P-glycoprotein (P-gp), encoded by MDR1 (ABCB1) gene, is a member of the ATP-binding cassette transporter protein superfamily that is constitutively expressed in the luminal membrane of the BBB. It protects brain tissue against small hydrophobic xenobiotics that can passively diffuse through the BBB by selectively transporting them from cells into the extracellular space [2]. Hence, P-gp may also limit or prevent the access of drugs, such as antiepileptics, antidepressants and anticancer drugs to their target sites in the brain [3]. Multiple lines of clinical and preclinical evidence suggest that enhanced P-gp function at the BBB may be responsible for drug resistance in several diseases [4], including epilepsy [5–7], depression [8, 9] and human immune deficiency syndrome [10]. Furthermore, altered P-gp function at the BBB has been proposed as a possible aetiology of neurodegenerative disease; e.g., decreased P-gp function is associated with a lower clearance of β-amyloid (Aβ) out of the brain, which would result in a predisposition for Aβ deposition in Alzheimer's disease (AD) [11–13]. A significant decrease of P-gp function in Parkinson's disease patients is likely to facilitate the accumulation of toxic compounds in the brain [14, 15].

Several potent P-gp substrates, including (*R*)-verapamil, have been labelled for imaging P-gp function with PET [16–18]. These substrates have high affinity for P-gp and because of efflux transport, a high brain uptake of the tracer reflects a decrease in P-gp function. However, they are not likely to measure overexpression of P-gp because the concentration of the tracer is already almost unmeasurable at baseline [16–18]. Besides low brain uptake of (*R*)-[^{11}C]verapamil, another disadvantage of this radiotracer is the formation of labelled metabolites that also act as P-gp substrate [19].

5-(1-(2-[^{18}F]fluoroethoxy))-[3-(6,7-dimethoxy-3,4-dihydro-1H-isoquinolin-2-yl)-propyl]-5,6,7,8-tetrahydronaphthalen ([^{18}F]MC225) has been developed as a selective substrate for P-gp with good metabolic stability [20] and has shown higher baseline brain uptake than that of other P-gp substrates in rodents [21] and non-human primates [22, 23]. These are suitable properties for measuring both increases and decreases in BBB P-gp function. These convincing results stimulated us to undertake an initial evaluation of [^{18}F]MC225 in human subjects as a phase 1 study.

The radiosynthesis of [^{18}F]MC225 was straightforward and met the GMP standards for human use [24]. The radiation absorbed dose estimated from mouse biodistribution data were the highest in the pancreas, but the effective dose was similar in magnitude to most other ^{18}F-labelled PET tracers [25]. The potential risk associated with [^{18}F]MC225 PET imaging is well within acceptable dose limits. The absence of any abnormalities in rats in the acute toxicity tests of MC225 and [^{18}F]MC225 injection and the absence of mutagenicity of MC225 together demonstrate the clinical suitability of [^{18}F]MC225 for the use in PET studies in humans [24].

The aim of the present first-in-human study of [^{18}F]MC225 was to examine the safety, radiation dosimetry and brain kinetics of [^{18}F]MC225 in healthy human subjects.

Materials and methods

Study design

This open-label phase 1 study was conducted using 2 cohorts (cohorts A and B). In cohort A, we estimated the biodistribution and whole-body dosimetry of [^{18}F]MC225. In cohort B, we measured [^{18}F]MC225 uptake in the brain and modelled radiotracer kinetics using radiometabolite-corrected arterial input function. The study protocol (Trial ID: jRCTs031190136) was approved by the Ministry of Health, Labour and Welfare-certified Clinical Research Review Board of the Tokyo Metropolitan Geriatric Medical Center (CRB3180026), and was performed in accordance with the World Medical Association Declaration of Helsinki. Written informed consent was obtained from all volunteer subjects prior to the study.

Study subjects and eligibility

Subjects were recruited using the healthy volunteer database of 3H Clinical Trial (Tokyo, Japan). Cohort A included 3 healthy male subjects (43.3 ± 10.7 years) and cohort B included 5 healthy male subjects (39.2 ± 13.2 years). For anatomical coregistration, MRI was performed in cohort B using a Discovery MR750w 3.0 T scanner (GE Healthcare, Milwaukee, WI). A 3-dimensional (3D) fast spoiled gradient-echo (repetition time, 7.6 ms; echo time, 3.1 ms; inversion time, 400 ms; matrix, 256 × 256 × 196 voxels) T1-weighted whole-brain image was acquired for each subject.

The main exclusion criteria in cohorts A and B were abnormal physical or neurological examination or paraclinical investigations (biochemistry, haematology and cardiovascular systems using standard laboratory tests and electrocardiograms), history of significant medical illness including major internal pathology or neurological and neuropsychiatric disorders, history of severe drug hypersensitivity,

smokers, significant abnormalities on anatomical MRI and the use of prescribed pharmaceuticals, general pharmaceuticals, quasi-drugs and health food products that induce, inhibit, or act as a substrate for P-gp. Subjects were asked to not drink alcohol on the day prior to the scan or on the scan day itself.

[^{18}F]MC225 synthesis

Radiosynthesis and quality control of [^{18}F]MC225 were performed as described previously [24]. [^{18}F]MC225 was obtained with radiochemical purity of 96.9% ± 0.6% (range, 95.8%–97.5%) and molar activity of 1074 ± 587 GBq/μmol (range, 122–1922 GBq/μmol) at the end of synthesis.

Subject dosing

No specific subject preparation such as fasting was requested prior to scanning. Subjects received an average dose of 186.5 ± 14.9 MBq (range, 163.5–211.8 MBq) of [^{18}F]MC225 over 1 min as a bolus via a catheterized antecubital vein. The average injected mass of [^{18}F]MC225 was 0.27 ± 0.31 μg (range, 0.09–1.03 μg) with average molar activity of 515 ± 303 GBq/μmol (range, 77–1078 GBq/μmol) at the time of injection. Table 1 lists the demographic data and dose information for all subjects in each study cohort.

Safety monitoring

Vital signs, including heart rate, pulse oximetry, blood pressure and body temperature were monitored pre- and post-administration of [^{18}F]MC225. Blood specimens were obtained and analysed (serum biochemistry and haematology analyses) before and at 7 days post-injection of [^{18}F]MC225. Adverse events were recorded on the day of [^{18}F]MC225 injection and throughout the follow-up period until day 7. The detailed protocol for investigating safety monitoring was the same as that reported previously [26].

Whole-body imaging

The protocol for investigating radiation dosimetry in human subjects using whole-body imaging was essentially the same as that reported previously [27]. Whole-body PET/CT was obtained using a Discovery MI PET/CT scanner (GE Healthcare) in 3D mode with an axial field of view 20.8 cm, spatial resolution of 3.91 mm in full width at half maximum (FWHM) and a z axis resolution of 4.50 mm in FWHM [28]. We acquired 431 slices for each 3D reconstruction.

Low-dose CT was used for attenuation and scatter correction of the PET emission scan. The first PET acquisition was started 1 min after the intravenous bolus injection of 190 ± 20 MBq (0.2–0.5 nmol) of [^{18}F]MC225. Whole-body scanning comprised 11-bed-position scans (overlap of 35 of 71 slices per bed position, 15 s/bed position × 4 frames, 30 s/bed position × 13 frames and 60 s/bed position × 3 frames) from the top of the head to midthigh. Further static images (120 s/bed position × 1 frame) were performed at 4 h and 6 h after injection. In between scans, the subjects were allowed to leave the scanner bed and urine was collected for measurement of radioactivity and determination of the metabolite fraction by high-performance liquid chromatography (HPLC). Whole-body data were reconstructed under the following conditions: 3D-ordered-subset–expectation maximization (3D-OSEM); 34 subsets; 2 iterations; Gaussian filter, 5.0 mm (FWHM); 128 matrix; field of view, 700 mm; 5.5 mm/pixel.

Regions of interest (ROIs) were placed manually over 17 organs that could be identified from PET or in the low-dose CT images: adrenals, brain, gallbladder, small intestine,

Table 1 Subject demographic data and dose information including net injected doses of [^{18}F]MC225 with corresponding injected mass, molar activity and plasma free fraction when appropriate

Volunteer number	Sex	Age (y)	Height (cm)	Weight (kg)	Activity (MBq)	Injected mass (μg)	MA (GBq/μmol)	Normalized injected mass (ng/kg)	f_P (%)
Cohort A									
1	M	55	169.8	78.6	188.0	0.21	408.5	2.72	
2	M	34	176.1	50.5	211.8	0.09	1077.7	1.69	
3	M	41	178.2	73.1	171.4	0.13	500.7	1.75	
Cohort B									
4	M	50	172.7	97.4	183.9	1.03	76.9	10.53	0.3
5	M	50	163.0	60.2	197.3	0.26	326.1	4.26	0.4
6	M	28	171.9	78.2	184.9	0.09	794.8	1.09	0.3
7	M	46	161.0	60.8	191.4	0.17	502.3	2.81	0.4
8	M	22	174.4	79.8	163.5	0.17	429.3	2.14	0.2

MA molar activity, f_P plasma free fraction

stomach, colon, heart wall, kidneys, liver, lungs, pancreas, bone marrow (thoracic and lumbar vertebrae), spleen, thymus, thyroid, testis and urinary bladder. The decay-uncorrected and decay-corrected time–activity curves (TACs) of organs were calculated as the percentage injected dose per organ. The normalized number of disintegrations (MBq-h/MBq administered) was then calculated for each source organ, which is equal to the area under the TAC multiplied by the volume of the organ ROI. The volume of bone marrow in which only part of the organ could be measured was substituted by the volume calculated from the mass of red marrow in the standard adult male phantom (1.12 kg for 73.7 kg of body weight), adjusted by the subject's body weight and 1 g/ml as the specific gravity [29]. The area under the TAC was calculated by summing the area from time 0 to the endpoint and the area from the endpoint to infinity of the uncorrected TACs. The former area was calculated by trapezoidal integration and the latter area was calculated by integration of radioactive decay from the endpoint.

The absorbed dose in 25 target organs of the adult male phantom was estimated from the normalized number of disintegrations of source organs by implementing the MIRD method using OLINDA/EXM (Vanderbilt University, Nashville, TN) [30]. The effective dose was calculated using the methodology described in the Recommendations of the International Commission on Radiological Protection (Publication 103) [31].

Brain PET scanning

PET scanning was performed using a Discovery MI PET/CT scanner (GE Healthcare). After low-dose CT scanning to correct for attenuation and scatter, [^{18}F]MC225 (164–197 MBq/0.2–2.4 nmol) was injected into the antecubital vein of each subject as a bolus for 1 min and a 90-min dynamic scan was then acquired in 3D mode (20 s × 3 frames, 30 s × 3 frames, 60 s × 5 frames, 150 s × 5 frames and 300 s × 14 frames). Arterial blood samples (each 0.5 ml) were obtained at 10, 20, 30, 40, 50, 60, 70, 80, 90, 100, 110, 120, 135, 150 and 180 s and also at 5, 7, 10, 15, 20, 30, 40, 50, 60, 75 and 90 min. The whole blood and separated plasma were weighed, and the radioactivity was measured with a NaI (Tl) well scintillation counter (BeWell Model-QS03 F/B; Molecular Imaging Labo, Suita, Japan). To analyse the labelled metabolites, an additional 1.5 ml of blood was obtained at 3-, 10-, 20-, 30-, 40- and 60-min scan durations. Free fractions (f_P) were determined by the ultrafiltration method as described previously [32].

After PET scanning, urine was obtained from each subject and radioactivity was measured. Unaltered [^{18}F]MC225 and radioactive metabolites in plasma were determined by HPLC.

Tomographic images were reconstructed using 3D-OSEM (16 subsets, 4 iterations) and incorporating time-of-flight information. The dynamic images were post-smoothed with a 3D-gaussian filter of 4 mm FWHM. The data were reconstructed in a 128 × 128 × 71 matrix and voxel size of 2.0 × 2.0 × 2.79 mm. Using the MRI obtained for coregistration for reference, partially overlapping circular ROIs of diameter 10 mm were placed on 9 brain regions: the frontal, temporal, parietal, occipital and cerebellar cortices and the thalamus, putamen, head of caudate nucleus and choroid plexus (Fig. 1a). TACs for these ROIs were calculated as Bq/ml or as standardized uptake value [SUV, (activity/ml tissue)/(injected activity/body weight)]. Using TACs of tissues and the metabolite-corrected TAC of plasma, we evaluated V_T for [^{18}F]MC225 using a 1-tissue-compartment model (1-TCM) (K_1/k_2) and a 2-tissue-compartment model (2-TCM) [$K_1/k_2 \times (1 + k_3/k_4)$]. PMOD (PMOD Technologies LLC, Zurich, Switzerland) was used in these evaluations. The blood delay of each subject was calculated using the mean TACs of the overall ROIs, and this value was then

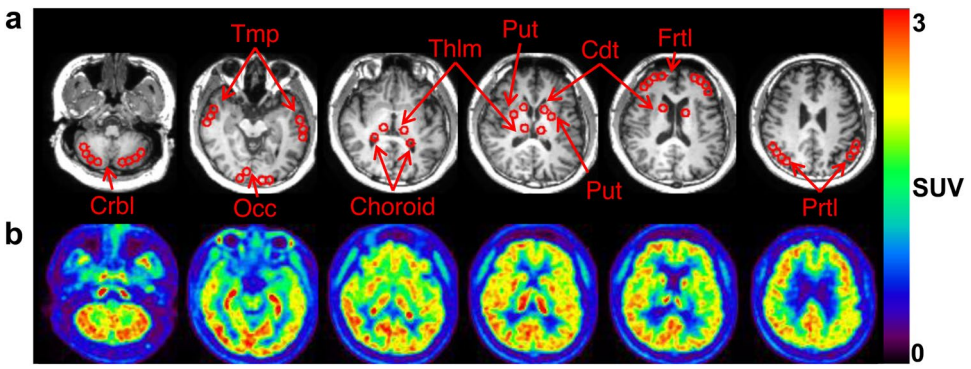

Fig. 1 Representative MR (**a**) and [^{18}F]MC225 PET (**b**) images summed from 20 to 40 min after injection ($SUV_{20\text{-}40\ min}$) obtained from subject number 4. The red circles on the MR images are regions of interest: Crbl = cerebellar cortex, Cdt = head of caudate nucleus, Choroid = choroid plexus, Frtl = frontal cortex, Occ = occipital cortex, Prtl = parietal cortex, Put = putamen, Thlm = thalamus, Tmp = temporal cortex

fixed for each ROI. All models were assessed both using a fixed (5%) fractional blood volume (vB) and using vB as a fit parameter. The goodness of fit by the 2-model analyses was evaluated using Akaike information criterion (AIC). V_T was also estimated by the Logan graphical method (Logan plot) ($t^* = 20$ min) [33] using in-house programs in MATLAB (MathWorks, MA). Additional surrogate PET kinetic parameters calculated without blood sampling were area under the curve (AUC) for the SUV of regional TACs from 0 to 60 min ($AUC_{0\text{-}60\ min}$), further subdivided into those from 0 to 30 min ($AUC_{0\text{-}30\ min}$) and those from 30 to 60 min ($AUC_{30\text{-}60\ min}$). The use of the negative slope calculated using the TACs has been proposed as a simplified method for measuring P-gp function [34, 35]. We also calculated the negative slope of the regional SUV TACs from 20 to 90 min after [^{18}F]MC225 injection. These surrogate parameters were compared with the V_T values as the reference parameters.

Metabolite analysis

Blood samples were collected at 3, 10, 20, 30, 40 and 60 min after the tracer injection; and urine was recovered at 149 ± 21 min (range, 134–173 min, $n = 3$). The samples were analysed by HPLC to determine the parent and metabolites of [^{18}F]MC225. The blood was centrifuged at 8700 g for 40 s at 2 °C to obtain plasma, which was denatured with an equivalent volume of 100% acetonitrile (final concentration, 50% acetonitrile) in an ice-water bath. The suspension was centrifuged using the same conditions and divided into soluble and precipitated fractions. The precipitate was resuspended in the same volume of 100% acetonitrile followed by centrifugation. This procedure was repeated twice. Radioactivity in the 3 soluble fractions and the precipitate was measured with an auto-γ-counter (Hidex AMG; Hidex, Turku, Finland). In this treatment of plasma, less than 8% of the total radioactivity is left in the final precipitation. The soluble fraction was combined and analysed by HPLC with a radioactivity detector (RAMONA Star; Elysia-raytest, Liège, Belgium). A YMC-Pack ODS-A column (10 mm inner diameter × 250 mm length; YMC, Kyoto, Japan) was used with acetonitrile/50 mM aqueous acetic acid/50 mM aqueous sodium acetate, pH 4.5 (74/13/13, v/v/v) at a flow rate of 4 ml/min. The retention time of [^{18}F]MC225 was 9.1 min. The urine samples were directly applied to HPLC.

Results

Safety monitoring

The administration of [^{18}F]MC225 was well tolerated by all subjects. There was no adverse or clinically detectable pharmacologic effect in any of the 8 subjects. No clinically important trend indicative of a safety signal was noted for any laboratory parameter, vital sign, or electrocardiogram parameter.

Whole-body imaging

A representative whole-body distribution of [^{18}F]MC225 is shown in Fig. 2 and decay-corrected TACs of source organs for the same subject are shown in Fig. 3. [^{18}F]MC225 was rapidly distributed in the brain, lung, heart, liver, pancreas, kidney, small intestine and bone marrow and decreased thereafter except in the liver and pancreas. Radioactivity of the liver and pancreas gradually increased up to 120 min and remained stable thereafter. Although the biodistribution implied hepatobiliary excretion, secretion of radioactivity from the liver to small intestine through the gallbladder was very slow. The total renal excreted radioactivity recovered during 6 h after injection was only < 2%ID (refer to the results of metabolite analysis).

Table 2 lists the organ-absorbed and effective doses. No organ showed a significant difference in absorbed dose between with urination and without urination. The highest absorbed dose was observed in the pancreas, followed by the liver, gallbladder wall, heart wall, small intestine, adrenals and kidneys. The mean effective dose with and without urination was calculated as 16.73 ± 1.03 and 16.77 ± 1.05 μSv/MBq, respectively.

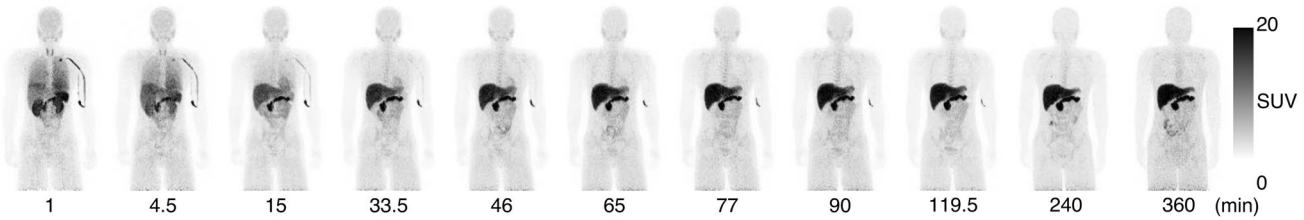

Fig. 2 Whole-body time–activity distribution of [^{18}F]MC225 in subject number 2, with representative decay-corrected maximum-intensity-projection images. PET image intensities are expressed as SUV. The time (min) indicates the start of whole-body scanning relative to [^{18}F]MC225 injection

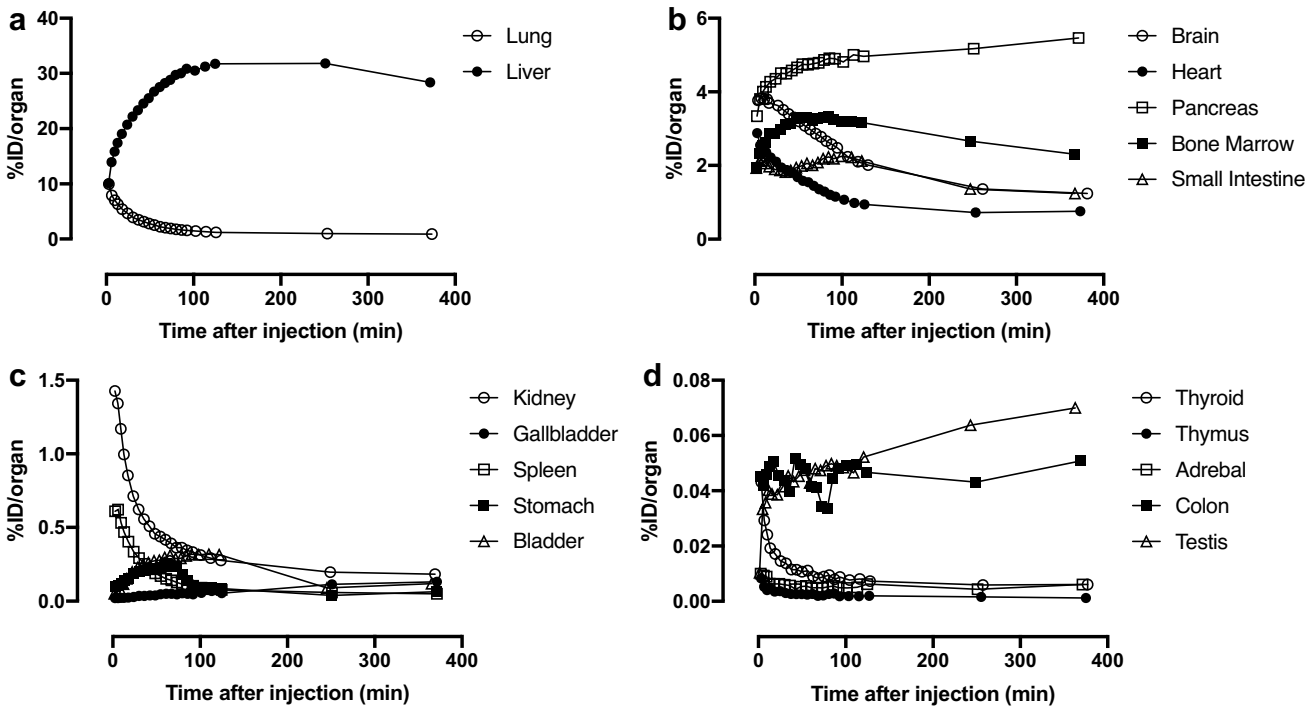

Fig. 3 Regional TACs of 17 source organs (**a**–**d**) after intravenous injection of [^{18}F]MC225 in the same subject as in Fig. 2. The panels show the TACs of source organs with high (**a**), moderate (**b**), low (**c**) and very low (**d**) radioactivity. Activities in bone marrow were estimated in the thoracic and lumbar vertebrae

Brain PET scanning

Figure 1 shows representative [^{18}F]MC225 images (Fig. 1b) and the corresponding MR images of the brain (Fig. 1a). [^{18}F]MC225 was homogeneously distributed among the grey matter. The appearance of laterality in brain uptake is caused by progressive widening of the sulci in the left brain on these slices. Figure 4 shows the mean TACs in the 9 brain regions after intravenous injection of [^{18}F]MC225. Individual peak uptake time of brain radioactivity varied widely. Averaged peak uptake of [^{18}F]MC225 in all 8 grey matter regions and in the choroid plexus was 6.5 ± 4.2 min (range, 1.8–16.3 min) and 5.7 ± 3.3 min (range, 3–11.3 min), respectively.

According to the AIC scores, the best fits were obtained when vB was used as a fit parameter (paired *t* test, $p < 0.0001$). The following analyses were performed using vB as the fit parameter, which provided values ranging between 1 and 8%. The preliminary kinetic analysis revealed that the 2-TCM provided lower AIC scores than did the 1-TCM. The standard errors of the estimated V_T values were much larger for the 1-TCM than the 2-TCM fit (paired *t* test, $p < 0.0001$). There were no significant differences or trends in V_T values when the left and right ROIs were analysed separately (Supplemental Fig. 1). Therefore, a merged region from both the left and right sides was used as each ROI. Table 3 lists the V_T values estimated by 1-TCM, 2-TCM and Logan plot. These values were compared by linear regression and Bland–Altman plots (Fig. 5). The correlation coefficient of linear regressions (Fig. 5a–c) was good ($r^2 > 0.9$), but the Bland–Altman plots revealed slightly more variation for 2-TCM versus Logan plot (Fig. 5f) than for 1-TCM versus 2-TCM (Fig. 5d) and 1-TCM versus Logan plot (Fig. 5e). The average difference between 1-TCM and 2-TCM and between Logan plot and 2-TCM was slightly negative (−0.280 and −0.144, respectively), meaning that V_T values obtained with 1-TCM and Logan plot were slightly lower than with 2-TCM fit (Fig. 5d, f). The SUV AUC values of the TACs were positively correlated with the V_T (2-TCM) values (r^2: $AUC_{0\text{-}60\ min} = 0.61$, $AUC_{0\text{-}30\ min} = 0.62$ and $AUC_{30\text{-}60\ min} = 0.59$, $p < 0.0001$) (Fig. 6a–c). The negative slope of the SUV TACs was negatively correlated with the V_T (2-TCM) values ($r^2 = 0.53$, $p < 0.0001$) (Fig. 6d).

Metabolite analysis

Plasma radioactivity rapidly decreased after bolus injection (Fig. 7a). The radioactivity concentration was higher in plasma than in whole blood (Fig. 7b).

Table 4 lists the results of the HPLC analysis of plasma. Two hydrophilic metabolites (HM1, 3.2 min and HM2, 5.7 min) were detected in plasma. At 60 min after injection,

Table 2 Organ-absorbed and effective doses of [^{18}F]MC225

Organ	Absorbed dose (μGy/MBq)	
	With urination	Without urination
Adrenals	18.03 ± 0.50	18.03 ± 0.50
Brain	9.84 ± 2.55	9.88 ± 2.59
Breasts	8.60 ± 0.29	8.64 ± 0.28
Gallbladder wall	27.10 ± 1.90	27.13 ± 1.90
Lower large intestine wall	11.13 ± 0.75	11.20 ± 0.75
Small intestine	19.27 ± 2.75	19.33 ± 2.72
Stomach wall	16.27 ± 0.31	16.30 ± 0.30
Upper large intestine wall	13.97 ± 0.45	14.07 ± 0.45
Heart walls	24.37 ± 5.85	24.43 ± 5.91
Kidneys	17.20 ± 2.80	17.23 ± 2.74
Liver	83.13 ± 11.24	83.17 ± 11.29
Lungs	16.40 ± 2.72	16.40 ± 2.72
Muscles	9.84 ± 0.37	9.93 ± 0.39
Ovaries	11.57 ± 0.55	11.60 ± 0.56
Pancreas	203.33 ± 44.77	203.33 ± 44.77
Red marrow	15.03 ± 0.25	15.13 ± 0.25
Osteogenic cells	16.87 ± 0.75	16.93 ± 0.72
Skin	7.30 ± 0.41	7.34 ± 0.40
Spleen	13.50 ± 2.54	13.53 ± 2.56
Testes	8.34 ± 1.71	8.37 ± 1.71
Thymus	8.88 ± 2.88	8.90 ± 2.86
Thyroid	7.75 ± 0.91	7.78 ± 0.91
Urinary bladder wall	11.63 ± 1.14	11.70 ± 1.08
Uterus	11.43 ± 0.60	11.50 ± 0.56
Total body	12.53 ± 0.06	12.63 ± 0.06
Effective dose (mSv/MBq)	16.73 ± 1.03	16.77 ± 1.05

The data obtained in healthy male subjects ($n = 3$), represented as mean ± SD

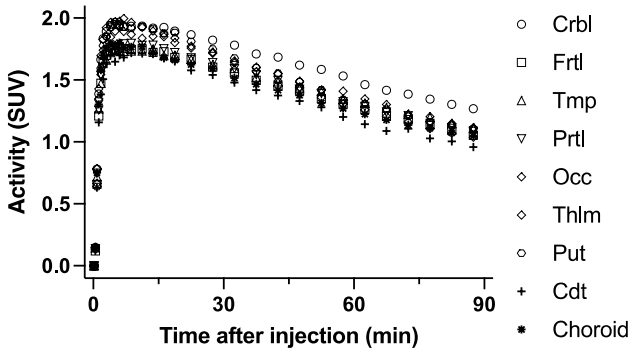

Fig. 4 Mean decay-corrected TACs of 9 brain regions after intravenous injection of [^{18}F]MC225. Crbl = cerebellar cortex, Frtl = frontal cortex, Tmp = temporal cortex, Prtl = parietal cortex, Occ = occipital cortex, Thlm = thalamus, Put = putamen, Cdt = head of caudate nucleus, Choroid = choroid plexus. The data represent the mean in 5 subjects. SD is not displayed for the sake of clarity

Table 3 [^{18}F]MC225 V_T estimated by 1-TCM, 2-TCM and Logan plot

Brain region	1-TCM	2-TCM	Logan plot
Cerebellar cortex	5.9 ± 1.3	6.2 ± 1.2	6.1 ± 1.2
Frontal cortex	4.9 ± 1.1	5.1 ± 1.1	5.1 ± 1.0
Temporal cortex	5.2 ± 1.2	5.5 ± 1.3	5.4 ± 1.2
Parietal cortex	5.1 ± 1.2	5.3 ± 1.2	5.2 ± 1.1
Occipital cortex	4.8 ± 1.1	5.0 ± 1.2	4.9 ± 1.1
Thalamus	5.1 ± 1.4	5.4 ± 1.5	5.3 ± 1.4
Putamen	5.0 ± 1.5	5.3 ± 1.5	5.1 ± 1.4
Caudate	4.4 ± 1.2	4.7 ± 1.4	4.5 ± 1.2
Choroid plexus	4.6 ± 1.6	5.0 ± 1.6	4.8 ± 1.6

1-TCM 1-tissue-compartment model, *2-TCM* 2-tissue-compartment model

The data obtained in healthy male subjects ($n = 5$), represented as mean ± SD

intact [^{18}F]MC225 remained dominant (54.8% ± 7.9%, $n = 5$). The present peripheral metabolism of [^{18}F]MC225 was slower than that reported in rats (15% of unmetabolized [^{18}F]MC225 at 60 min) [20] and in non-human primates (28% of unmetabolized [^{18}F]MC225 at 60 min) [22]. The mean radioactivity voided into urine at 101 ± 3 min (range, 97–104 min, $n = 4$) and the cumulative voided radioactivity into urine at 351 ± 35 min (range, 316–386 min, $n = 3$) were 0.5% ± 0.1% (range, 0.3–0.6%, $n = 4$) and 1.8% ± 0.1% (range, 1.7–1.9%, $n = 3$) of injected activity, respectively. In urine, the hydrophilic metabolites HM1 (82.9% ± 4.6%, $n = 3$) and HM2 (17.1% ± 4.6%, $n = 3$) were observed, though the parent radioligand was not detected.

The f_P of [^{18}F]MC225 was very low (0.32% ± 0.08%, $n = 5$). The ultrafiltrate-to-saline ratio was 68% ± 3% ($n = 5$), indicating high retention of [^{18}F]MC225 on the filter.

Discussion

This is the first clinical study to assess the safety, radiation dosimetry and initial brain imaging of [^{18}F]MC225 in a small population of healthy human subjects.

We determined [^{18}F]MC225 to be safe and well tolerated, with no adverse effects in the 8 subjects included in this study. Because PET tracers are administered intravenously as a bolus, it is important to consider their potential hazard to the cardiovascular system. However, the highest administered dose (10.53 ng/kg) was below 1/40,000 of the potential vasodilator and cardiotoxic dose of MC225 [36].

There was no significant difference of absorbed dose between with and without urination for any organ. The most critical organ was the pancreas, which had absorbed dose of 203 μGy/MBq, corresponding to 38 mGy of absorbed dose when 185 MBq of [^{18}F]MC225 was administered. Most

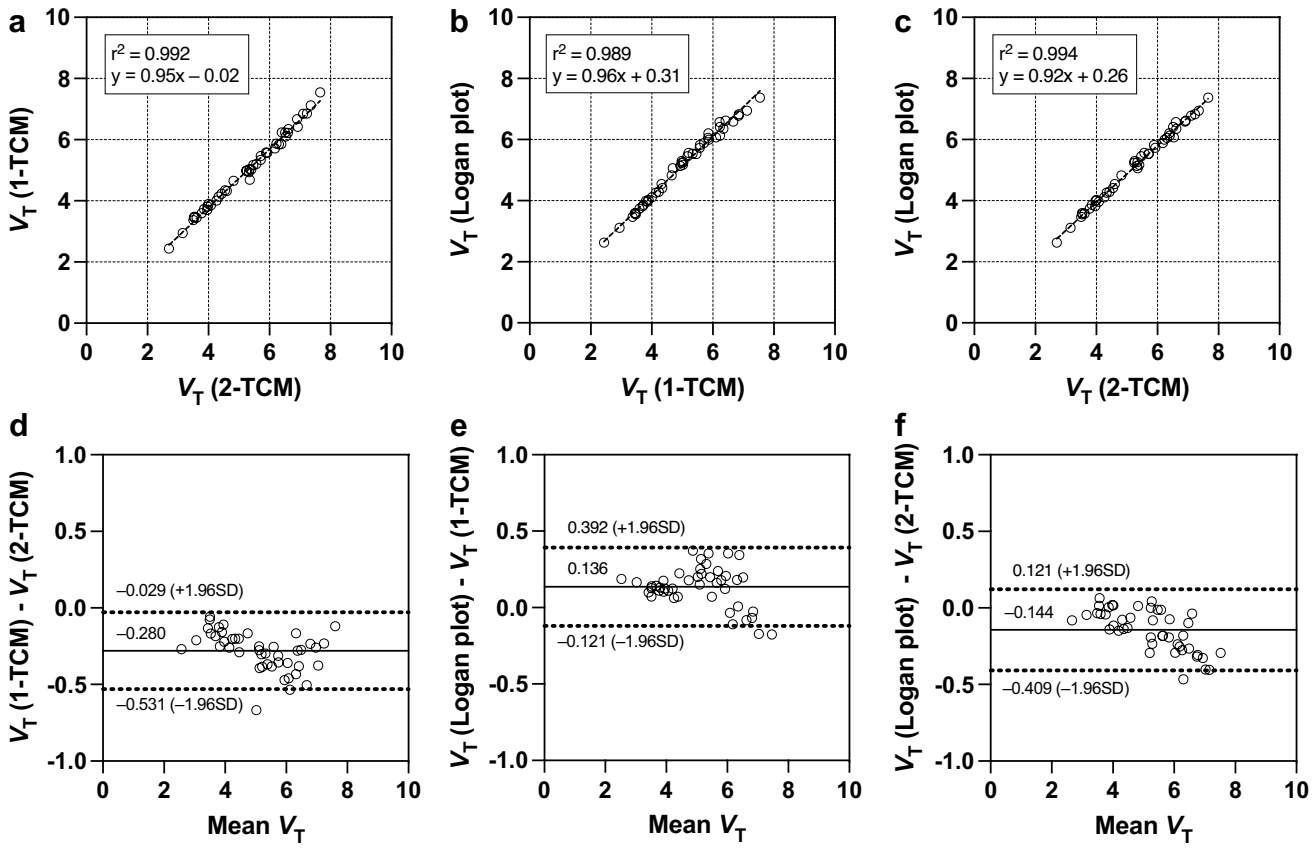

Fig. 5 Comparison of V_T data calculated in different ways: correlation of (**a**) 2-TCM fit versus 1-TCM fit, (**b**) 1-TCM versus Logan plot and (**c**) 2-TCM versus Logan plot. All fits used metabolite-corrected plasma radioactivity as the input. Bland–Altman plots with 95% confidence intervals represent the difference of V_T versus mean V_T, for (**d**) 2-TCM fit versus 1-TCM fit, (**e**) 1-TCM versus Logan plot and (**f**) 2-TCM versus Logan plot

central nervous system drugs are lipophilic weak basic compounds. Those such as [^{18}F]MC225 are favourably absorbed in the pancreas, which contains abundant alkaline pancreatic juice, for the reason that basic compounds cannot be ionized in basic medium.

Other organs with high values of absorbed radiation were excretory organs, such as the liver, gallbladder wall, small intestine and kidneys. Interestingly, absorbed dose was also high in the heart walls and adrenals; this can be explained by the fact that [^{18}F]MC225 possesses a 6,7-dimethoxy-1,2,3,4-tetrahydroisoquinoline substructure, which has weak agonistic or antagonistic activities on the β-adrenoceptor [37].

The mean effective doses with and without urination were calculated as 16.7 and 16.8 μSv/MBq, respectively, which correspond to 3.1 mSv of effective dose when 185 MBq of [^{18}F]MC225 was administered. The effective dose of 3.1 mSv/185 MBq is within the strict limit of 10 mSv set in the ICRP recommendations [38]. Moreover, the highest dose in the pancreas of 38 mGy/185 MBq is also within the strict limit for individual organs set in the US Radioactive Drug Research Committee regulations [39]. Although the rate of [^{18}F]MC225 excretion in urine was significantly slower in humans than in mice, in terms of effective dose, the discrepancy was small between those extrapolated from mouse biodistribution data (15.7 and 16.9 μSv/MBq with and without urination, respectively) [24] and those in the present human study. Organ-absorbed doses in the liver, gallbladder wall, pancreas and heart wall were 2 to 3 times higher than those estimated from the mouse biodistribution study. In contrast, the present organ-absorbed doses in the small intestine, large intestine wall and urinary bladder wall were 1/2 to 1/5 lower than those estimated from the mouse study. This might be due to the slower hepatobiliary and urine excretion of radioactivity in humans than in mice. Other organ-absorbed doses determined in the present human study are mostly equivalent to those estimated from the mouse study.

The slower hepatobiliary and urine clearance of radioactivity might be caused by the slower peripheral metabolism of [^{18}F]MC225 in humans than in rodents. P-gp is expressed on the luminal side of the capillary endothelial cells in the brain. In contrast, P-gp is expressed on the opposite side of the epithelial lumen in extra-brain tissues, such as the

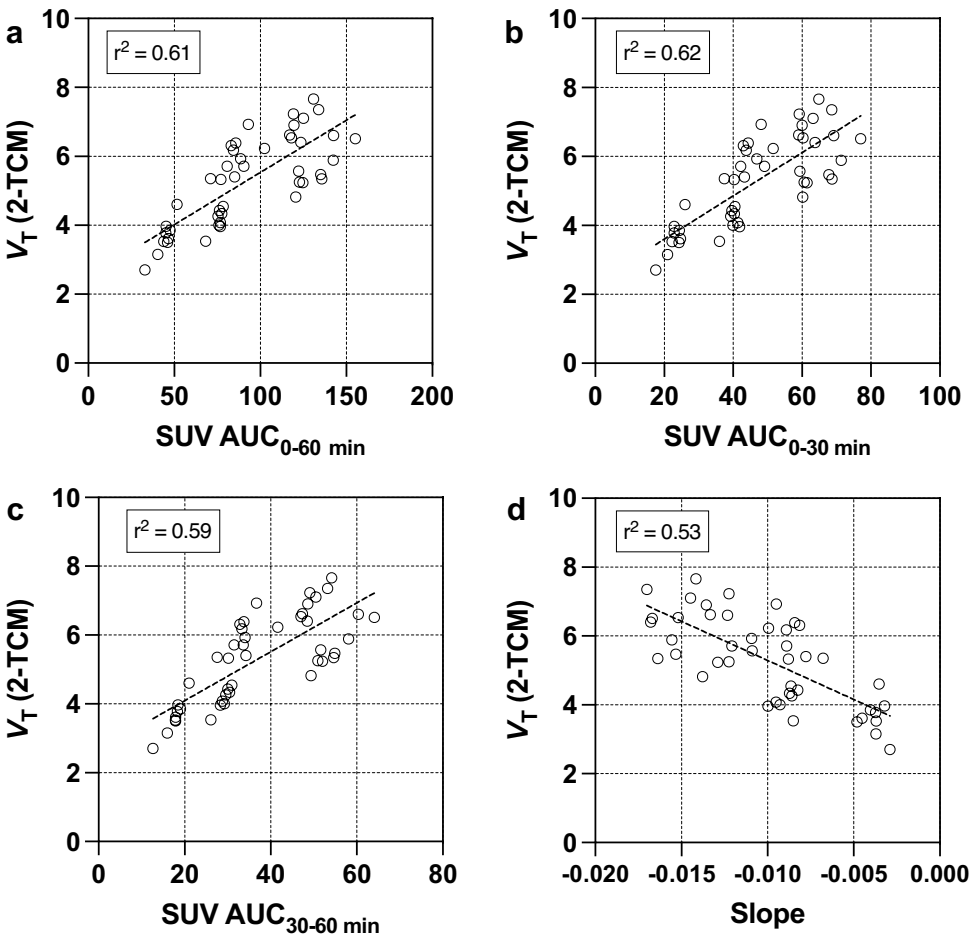

Fig. 6 Correlation between V_T (2-TCM) and simplified surrogate parameters: correlation of (**a**) SUV $AUC_{0\text{-}60\ min}$ versus V_T (2-TCM), (**b**) SUV $AUC_{0\text{-}30\ min}$ versus V_T (2-TCM), (**c**) SUV $AUC_{30\text{-}60\ min}$ versus V_T (2-TCM) and (**d**) negative slope of the SUV TACs versus V_T (2-TCM)

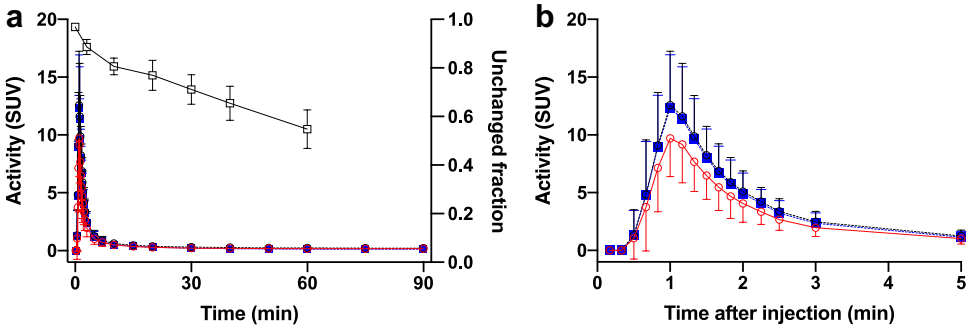

Fig. 7 Mean decay-corrected TACs of whole blood (open red circles), plasma (open black circles), metabolite corrected plasma (closed blue squares) and unchanged fraction of [^{18}F]MC225 (open black squares) after intravenous injection of [^{18}F]MC225 into human subjects (**a**). Values for 5 min (**b**) extracted from **a**. The data represent the mean ± SD in 5 subjects

intestine, liver and kidney; i.e., in bile canaliculi, intestinal lumen and proximal tubule lumen [40]. When [^{18}F]MC225 is delivered from the capillaries to hepatocytes, intestinal epithelia and distal convoluted tubular epithelial cells, [^{18}F]MC225 itself is excreted to the intestinal lumen, bile and urine. However, clearance of the radioactivity from these organs is very slow. In urine, only hydrophilic metabolite was detected and [^{18}F]MC225 itself was not detected, meaning that most of the intracellular trapped [^{18}F]MC225 may not exist as its free form: substrate for P-gp. A possible explanation for these slow kinetics in peripheral organs could be the presence of unknown trapping mechanisms of [^{18}F]MC225, including generation of a retentive intermediate metabolite; non-specific binding to membrane, lipid and protein; and the existence of an off-target binding site, among others.

Table 4 Percentages of radiolabelled metabolites in plasma after intravenous injection of [^{18}F]MC225

Time (min)	HM1	HM2	[^{18}F]MC225
3	4.1 ± 1.1	6.8 ± 3.5	88.6 ± 3.1
10	11.3 ± 3.1	6.8 ± 2.0	80.6 ± 3.4
20	16.8 ± 5.9	4.9 ± 1.5	77.0 ± 6.2
30	24.3 ± 5.2	3.5 ± 0.8	71.1 ± 6.1
40	30.0 ± 6.9	2.5 ± 1.3	65.5 ± 7.1
60	40.4 ± 7.8	3.7 ± 1.3	54.8 ± 7.9

HM hydrophilic metabolite

The data obtained in healthy male subjects ($n = 5$), represented as mean ± SD

[^{18}F]MC225 was widely and homogeneously distributed in brain grey matter regions. We selected V_T as an outcome measure of P-gp function [18]. Because [^{18}F]MC225 is a weak P-gp substrate, it is only partially transported by P-gp across the BBB and may either enter the brain (and possibly interact with other brain structures) or be transported back to the blood by P-gp. In this case, the efflux rate constant k_2 can be interpreted as a measure of P-gp function. As k_2 can be blood flow dependent, V_T can be used as an alternative measure of P-gp function that would obviate the need for separate blood flow measurements. In a previous study, both K_1 and V_T were used to estimate P-gp function at the BBB in non-human primates [22]. In the case of [^{18}F]MC225 being immediately transported back to the blood by P-gp, K_1 can be interpreted as a measure of P-gp function. However, K_1 is blood flow dependent and correct interpretation of the results may require separate measurements of cerebral blood flow.

The f_P values were consistently very low (< 0.4%), and there was evidence that [^{18}F]MC225 had adhered to the ultrafiltration tubes and/or membrane, which may have led to underestimation of f_P. Normalization of V_T by f_P results in unusually high values (> 1000) and hence was not applied in this study.

In this preliminary study, we observed large individual differences of V_T in the grey matter regions and choroid plexus. The coefficient of variation (CV) of interindividual V_T in 1-TCM, 2-TCM and Logan plot was 26% ± 4%, 26% ± 4% and 24% ± 4%, respectively. In contrast, intraindividual differences of V_T in these regions were relatively small: the CV of intraindividual V_T in 1-TCM, 2-TCM and Logan plot was 11% ± 3%, 11% ± 3% and 10% ± 3%, respectively. The large interindividual variances can be attributed to individual differences in P-gp density and/or function. Many factors are considered to possibly affect P-gp expression and function, among which several lines of evidence have suggested that the abundance and activity of P-gp at the human BBB decreases with increasing age [41–45]. This theory is in agreement with the present finding of higher V_T (2-TCM) values of [^{18}F]MC225 in the grey matter regions of 3 middle-aged subjects when compared with those in the 2 youngest subjects (Supplemental Fig. 2).

Another point for consideration is the diurnal variation in P-gp function [46], which has been detected at the BBB using [^{18}F]MC225 in rats [47]. In the present study, [^{18}F]MC225 was administered in cohort B at 10:00 am in 1 subject and at 13:00–14:00 pm in the other 4 subjects. There was no trend between injection time and V_T in this small cohort.

Although we did not observe any effect of body mass index on the V_T of [^{18}F]MC225 in our small sample, increased body mass index is associated with reduced expression of P-gp in the human brain [48]. Interestingly, low-density lipoprotein receptor-related 1 and P-gp are altered in diabetes mellitus (DM) [49]. These molecules cooperate in the clearance of extracellular Aβ from brain parenchyma to the capillaries [50]. P-gp has been identified not only in BBB, but also in neuronal cells, astrocytes and microglia [51]. Furthermore, oxidative stress [52] and neuroinflammation [53], which are observed in several neurodegenerative diseases, including AD, can modulate P-gp expression. Because DM is a risk factor for cognitive impairment (including AD) and BBB dysfunction [54, 55], the mutual relationships of DM and neuroinflammation to Aβ and P-gp function are of great interest.

A limitation of this study is the lack of analysis of MDR1 gene polymorphism in the subjects. Several single nucleotide polymorphisms (SNPs) have been reported for the MDR1 gene, which encodes P-gp. A synonymous C3435T polymorphism in exon 26 was reported to be associated with a lower expression level of P-gp in the duodenum [56]. However, the contribution of MDR1 variants to the expression of P-gp (both at protein and mRNA levels) remains controversial. Several previous quantitative analyses of P-gp function with [^{11}C]verapamil at the BBB did not support evidence that C3435 SNPs in exon 26 MDR1 gene haplotypes (3 SNPs: C1236T, G2677T and C3435T) influence the kinetics of [^{11}C]verapamil [44, 57, 58].

We found a moderate correlation between V_T (2-TCM) and SUV AUC of TACs ($r^2 \geq 0.59$) than between V_T (2-TCM) and negative slope of SUV TACs ($r^2 = 0.53$). $AUC_{30\text{-}60\ min}$ might be preferable because $AUC_{0\text{-}30\ min}$ is more likely to be affected by variability in plasma and brain kinetics at early time points. A simplified surrogate parameter that does not require arterial blood sampling and has a short scan duration is clearly preferable in the clinical setting. However, the analytical time frame in the present study was not fully optimized and further validation is necessary in test–retest and in drug-loading studies.

The present V_T values in grey matter were significantly higher than for any other previously developed strong P-gp

substrate tracer [16–18] and currently studied weak substrate [34, 35]. [^{18}F]MC225 is the first clinically available ^{18}F-labelled P-gp substrate and the brain images are better than for previously evaluated ^{11}C-labelled P-gp substrate because of the higher brain uptake and higher counting statistics for ^{18}F radionuclide. It is necessary in future studies to determine whether [^{18}F]MC225 can detect functional impact on disease-induced reduction or induction of P-gp at the BBB and to conduct further test–retest and drug-loading validation of [^{18}F]MC225. These validation studies are currently ongoing and preliminary impressive drug-loading images have been reported [59].

There are numerous possible clinical applications of [^{18}F]MC225. For example, [^{18}F]MC225 PET can predict drug resistance in patients with brain tumours, epilepsy and treatment-resistant psychiatric illness. Consequently, [^{18}F]MC225 PET might inform physicians of the potential pharmacokinetic action of viable medication. P-gp expression begins to decline in middle-aged cognitively healthy individuals, leading to gradual Aβ accumulation [43]. Hence, imaging P-gp function at the BBB in the very early stages of Aβ depositions is of crucial importance. [^{18}F]MC225 PET may be a valuable tool for identifying the very early phases of AD progression. There is no doubt early intervention is critical and restoring defective transport-mediated clearance to prevent initial deposition of Aβ may slow or halt disease progression. Enhancing the expression and function of P-gp in the brain could present as an effective therapeutic strategy to reduce levels of neurotoxic Aβ species in AD. [^{18}F]MC225 PET can be applied to monitor the effect of P-gp inducers which promote the clearance of Aβ from the brain. The ability of [^{18}F]MC225 to measure increases in P-gp function has been confirmed in a study that reported that the administration of a P-gp inducer to healthy rats decreased the V_T and K_1 values of [^{18}F]MC225 compared with controls [60].

Conclusions

The initial findings of the present study in a small group of subjects indicated that [^{18}F]MC225 PET is feasible for imaging P-gp function in the brain, and has acceptable radiation dose and pharmacological safety at the dose required for adequate PET imaging. The brain uptake of [^{18}F]MC225 can be calculated as V_T as an indicator of BBB P-gp function. The V_T values in grey matter are significantly higher than those of any P-gp tracers ever developed; therefore, [^{18}F]MC225 might be a suitable PET tracer for measuring both increases and decreases of P-gp function. A simplified parameter such as AUC of TACs may be used as an alternative to V_T. We expect that these positive findings will lead to further application of [^{18}F]MC225 to the evaluation of altered P-gp function at the BBB in patient populations. To enable such applications, test–retest and drug-loading studies are required to fully validate the quantification method of P-gp function with [^{18}F]MC225.

Supplementary Information The online version contains supplementary material available at https://doi.org/10.1007/s12149-021-01666-9.

Acknowledgements We thank Mr. Masanari Sakai and Mr. Kosuke Nishino for technical support with cyclotron operation and radiosynthesis, Ms. Kimiko Yokoyama and Ms. Kazuko Takagi for care of the subjects during PET scanning and Ms. Airin Onishi for coordination of the clinical study.

Funding This work was supported in part by Grants-in-Aid for Scientific Research (C) Nos. 18K07658 and 21K07663 from the Japan Society for the Promotion of Science.

Data availability The datasets generated during and analysed during the current study are available from the corresponding author on reasonable request.

Code availability Not applicable.

Declarations

Conflicts of interest The authors have no relevant financial or non-financial interests to disclose.

Ethics approval All procedures performed in studies involving human participants were approved by the Ministry of Health, Labour and Welfare Certified Clinical Research Review Board, Tokyo Metropolitan Geriatric Medical Center (CRB3180026) and in accordance with the principles of the 1964 Declaration of Helsinki and its later amendments.

Consent to participate Written informed consent was obtained from all individual participants prior to their inclusion in the study.

Consent to publication Not applicable.

References

1. Terasaki T, Ohtsuki S. Brain-to-blood transporters for endogenous substrates and xenobiotics at the blood-brain barrier: an overview of biology, and methodology. NeuroRx. 2005;2:63–72.
2. Giacomini KM, Huang S-M. Transporters in drug development and clinical pharmacology. Clin Pharmacol Ther. 2013;94:3–9.
3. Graff CL, Pollack GM. Drug transporter at the blood–brain barrier and the choroid plexus. Curr Drug Metab. 2004;5:95–108.
4. Löscher W, Potschka H. Drug resistance in brain disease and the role of drug efflux transporters. Nat Rev Neurosci. 2005;6:591–602.
5. Feldmann M, Koepp M. ABC transporter and drug resistance in patients with epilepsy. Curr Pharm Des. 2016;22:5793–807.
6. Ilyas-Feldmann M, Asselin M-C, Wang S, McMahon A, Anton-Rodriguez A, Brown G, et al. P-glycoprotein overactivity in epileptogenic developmental lesions measured in vivo using (*R*)-[^{11}C]verapamil PET. Epilepsia. 2020;61:1472–80.

7. Volk HA, Löscher W. Multidrug resistance in epilepsy: rats with drug-resistant seizures exhibit enhanced brain expression of P-glycoprotein compared with rats with drug-responsive seizures. Brain. 2005;128:1358–68.
8. O'Brien FE, Clarke G, Fitzgerald P, Dinan TG, Griffin BT, Cryan JF. Inhibition of P-glycoprotein enhances transport of imipramine across the blood-brain barrier: microdialysis studies in conscious freely moving rats. Br J Pharmacol. 2012;166:1333–43.
9. de Klerk OL, Willemsen AT, Roosink M, Bartels AL, Hendrikse NH, Bosker FJ, et al. Locally increased P-glycoprotein function in major depression: a PET study with [^{11}C]verapamil as a probe for P-glycoprotein function in the blood–brain barrier. Int J Neuropsychopharmacol. 2009;12:895–904.
10. Kim RB, Fromm MF, Wandel C, Leake B, Wood AJ, Roden DM, et al. The drug transporter P-glycoprotein limits oral absorption and brain entry of HIV-protease inhibitors. J Clin Invest. 1998;101:289–94.
11. Chai AB, Leung GKF, Callaghan R, Gelissen IC. P-glycoprotein: a role in the export of amyloid-β in Alzheimer's disease? FEBS J. 2020;287:612–25.
12. Deo AK, Borson S, Link JM, Domino K, Eary JF, Ke B, et al. Activity of p-glycoprotein, a β-amyloid transporter at the blood–brain barrier, is compromised in patients with mild Alzheimer disease. J Nucl Med. 2014;55:1106–11.
13. van Assema DME, Lubberink M, Bauer M, van der Filer WM, Schuit RC, Windhorst AD, et al. Blood–brain barrier P-glycoprotein function in Alzheimer's disease. Brain. 2012;135:181–9.
14. Bartels AL, Willemsen ATM, Kortekaas R, de Jong BM, de Vries R, de Klerk O, et al. Decreased blood–brain barrier P-glycoprotein function in the progression of Parkinson's disease PSP and MSA. J Neural Transm (Vienna). 2008;115:1001–9.
15. Vautier S, Fernandez C. ABCB1: the role in Parkinson's disease and pharmacokinetics of antiparkinsonian drugs. Expert Opin Drug Metab Toxicol. 2009;5:1349–58.
16. Luurtsema G, Elsinga P, Dierckx R, Boellaard R, van Waarde A. PET tracers for imaging of ABC transporters at the blood–brain barrier: principles and strategies. Curr Pharm Des. 2016;22:5779–85.
17. Raaphorst RM, Windhorst AD, Elsinga PH, Colabufo NA, Lammertsma AA, Luurtsema G. Radiopharmaceuticals for assessing ABC transporters at the blood–brain barrier. Clin Pharmacol Ther. 2015;97:362–71.
18. Lubberink M. Kinetic models for measuring P-glycoprotein function at the blood-brain barrier with positron emission tomography. Curr Pharm Des. 2016;22:5786–92.
19. Luurtsema G, Molthoff CFM, Schuit RC, Windhorst AD, Lammertsma AA, Franssen EJF. Evaluation of (*R*)-[^{11}C]verapamil as PET tracer of P-glycoprotein function in the blood–brain barrier: kinetics and metabolism in the rat. Nucl Med Biol. 2005;32:87–93.
20. Savolainen H, Windhorst AD, Elsinga PH, Cantore M, Colabufo NA, Willemsen AT, et al. Evaluation of [^{18}F]MC225 as a PET radiotracer for measuring P-glycoprotein function at the blood–brain barrier in rats: kinetics, metabolism, and selectivity. J Cereb Blood Flow Metab. 2017;37:1286–98.
21. Savolainen H, Cantore M, Colabufo NA, Elsinga PH, Windhorst AD, Luurtsema G. Synthesis and preclinical evaluation of three novel fluorine-18 labeled radiopharmaceuticals for P-glycoprotein PET imaging at the blood–brain barrier. Mol Pharm. 2015;12:2265–75.
22. García-Varela L, Arif WM, García DV, Kakiuchi T, Ohba H, Harada N, et al. Pharmacokinetic modeling of [^{18}F]MC225 for quantification of the P-glycoprotein function at the blood–brain barrier in non-human primates with PET. Mol Pharm. 2020;17:3477–86.
23. García-Varela L, García DV, Aguiar P, Kakiuchi T, Ohba H, Harada N, et al. Head-to-head comparison of (*R*)-[^{11}C]verapamil and [^{18}F]MC225 in non-human primates, tracers for measuring P-glycoprotein function. Eur J Nucl Med Mol Imaging. 2021. https://doi.org/10.1007/s00259-021-05411-2.
24. Toyohara J, Sakata M, Tago T, Colabufo NA, Luurtsema G. Automated synthesis, preclinical toxicity, and radiation dosimetry of [^{18}F]MC225 for clinical use: a tracer for measuring P-glycoprotein function at the blood–brain barrier. EJNMMI Res. 2020;10:84.
25. Zanotti-Fregonara P, Lammertsma AA, Innis RB. Suggested pathway to assess radiation safety of ^{18}F-labeled PET tracers for first-in-human studies. Eur J Nucl Med Mol Imaging. 2013;40:1781–3.
26. Toyohara J, Sakata M, Oda K, Ishii K, Ito K, Hiura M, et al. Initial human PET studies of metabotropic glutamate receptor type 1 ligand ^{11}C-ITMM. J Nucl Med. 2013;54:1302–7.
27. Ito K, Sakata M, Oda K, Wagatsuma K, Toyohara J, Ishibashi K, et al. Comparison of dosimetry between PET/CT and PET alone using ^{11}C-ITMM. Austr Phys Eng Sci Med. 2016;39:177–86.
28. Wagatsuma K, Miwa K, Sakata M, Oda K, Ono H, Kameyama M, et al. Comparison between new-generation SiPM-based and conventional PMT-based TOF-PET/CT. Phys Med. 2017;42:203–10.
29. Kirschner AS, Ice RD, Beierwaltes WH. Radiation dosimetry of ^{131}I–19-iodo-cholesterol: the pitfalls of using tissue concentration data reply. J Nucl Med. 1975;16:248–9.
30. Stabin MG, Sparks RB, Crowe E. OLINDA/EXM: the second-generation personal computer software for internal dose assessment in nuclear medicine. J Nucl Med. 2005;46:1023–7.
31. ICRP. The 2007 recommendations of the international commission on radiological protection ICRP publication 103. Ann ICRP. 2007;37:1–332.
32. Toyohara J, Yamamoto H, Tago T. Searching for diagnostic properties of novel fluorine-18-labeled D-allose. Ann Nucl Med. 2019;33:855–65.
33. Logan J, Fowler JS, Volkow ND, Wolf AP, Dewey SL, Schlyer DJ, et al. Graphical analysis of reversible radioligand binding from time–activity measurement applied to [*N*-^{11}C-methyl]-(–)-cocaine PET studies in human subjects. J Cereb Blood Flow Metab. 1990;10:740–7.
34. Auvity S, Caillé F, Marie S, Wimberley C, Bauer M, Langer O, et al. P-Glycoprotein (ABCB1) inhibits the influx and increases the efflux of ^{11}C-metoclopramide across the blood–brain barrier: a PET study on nonhuman primates. J Nucl Med. 2018;59:1609–15.
35. Tournier N, Bauer M, Picher V, Nics L, Klebermass E-M, Bamminger K, et al. Impact of P-glycoprotein function on the brain kinetics of the weak substrate ^{11}C-metoclopramide assessed with PET imaging in humans. J Nucl Med. 2019;60:985–91.
36. Fusi F, Durante M, Gorelli B, Perrone MG, Colabufo NA, Saponara S. MC225, a novel probe for P-glycoprotein PET imaging at the blood–brain barrier: in vitro cardiovascular safety evaluation. J Cardiovasc Pharmacol. 2017;70:405–10.
37. Brzezińska E. Synthesis and pharmacological properties of 6,7-dimethoxy-1,2,3,4-tetrahydroisoquinoline derivatives. Acta Pol Pharm. 1996;53:365–71.
38. ICRP. Radiological protection in biomedical research. ICRP Publication 62. Ann ICRP. 1992;22:1–18.
39. RDRC Final Guidance: human research without an investigational new drug application. 2010 https://www.fda.gov/media/76286/download. (Accessed Aug 2010).
40. Staud F, Ceckova M, Micuda S, Pavek P. Expression and function of P-glycoprotein in normal tissues: effect on pharmacokinetics. Methods Mol Biol. 2010;596:199–222.
41. Bartels A, Kortekaas R, Bart J, Willemsen ATM, de Klerk OL, de Vries JJ, et al. Blood–brain barrier P-glycoprotein function decreases in specific brain regions with aging: a possible role in progressive neurodegeneration. Neurobiol Aging. 2009;30:1818–24.

42. Bauer M, Karch R, Neumann F, Abrahim A, Wagner CC, Kletter K, et al. Age dependency of cerebral P-gp function measured with (*R*)-[^{11}C]verapamil PET. Eur J Clin Pharmacol. 2009;65:941–6.
43. Chiu C, Miller MC, Monahan R, Osgood DP, Stopa EG, Silverberg GD. P-glycoprotein expression and amyloid accumulation in human aging and Alzheimer's disease: preliminary observations. Neurobiol Aging. 2015;36:2475–82.
44. Toornvliet R, van Berckel BNM, Luurtsema G, Lubberink M, Geldof AA, Bosch TM, et al. Effect of age on functional P-glycoprotein in the blood–brain barrier measured by use of (*R*)-[^{11}C] verapamil and positron emission tomography. Clin Pharmacol Ther. 2006;79:540–8.
45. van Assema DME, Lubberink M, Boellaard R, Schuit RC, Windhorst AD, Scheltens P, et al. P-glycoprotein function at the blood–brain barrier: effects of age and gender. Mol Imaging Biol. 2012;14:771–6.
46. Kervezee L, Hartman R, van den Berg D-J, Shimizu S, Emoto-Yamamoto Y, Meijer JH, et al. Diurnal variation in P-glycoprotein-mediated transport and cerebrospinal fluid turnover in the brain. AAPS J. 2014;16:1029–37.
47. Savolainen H, Meerlo P, Elsinga PH, Windhorst AD, Dierckx RAJO, Colabufo NA, et al. P-glycoprotein function in the rodent brain displays a daily rhythm, a quantitative in vivo PET study. AAPS J. 2016;18:1524–31.
48. Vendelbo J, Olesen RH, Lauridsen JK, Rungby J, Kleinman JE, Hyde TM, et al. Increasing BMI is associated with reduced expression of P-glycoprotein (ABCB1 gene) in the human brain with a stronger association in African Americans than Caucasians. Pharmacogenomics J. 2018;18:121–6.
49. Banks WA. The blood–brain barrier interface in diabetes mellitus: dysfunctions, mechanisms and approaches to treatment. Curr Pharm Des. 2020;26:1438–47.
50. Strock SE, Hartz AMS, Bernard J, Wolf A, Kachlmeier A, Mahringer A, et al. The concerted amyloid-beta clearance of LRP1 and ABCB1/P-gp across the blood-brain barrier is linked by PICALM. Brain Behav Immun. 2018;73:21–33.
51. Sanchez-Covarrubias L, Slosky LM, Thompson BJ, Davis TP, Ronaldson PT. Transporters at CNS barrier sites: obstacles or opportunities for drug delivery? Curr Pharm Des. 2014;20:1422–49.
52. Sita G, Hrelia P, Tarozzi A, Morroni F. P-glycoprotein (ABCB1) and oxidative stress: focus on Alzheimer's disease. Oxid Med Cell Longev. 2017;2017:7905486.
53. Alasmari F, Ashby CR Jr, Hall FS, Sari Y, Tiwari AK. Modulation of the ATP-binding cassette B1 transporter by neuro-inflammatory cytokines: role in pathogenesis of Alzheimer's disease. Front Pharmacol. 2018;9:658.
54. Pugazhenthi S, Qin L, Reddy PH. Common neurodegenerative pathway in obesity, diabetes, and Alzheimer's disease. Biochem Biophys Acta Mol Basis Dis. 2017;1863:1037–45.
55. Goldwaser EL, Acharya NK, Sarkar A, Godsey G, Nagele RG. Breakdown of the cerebrovasculature and blood–brain barrier: a mechanistic link between diabetes mellitus and Alzheimer's disease. J Alzheimers Dis. 2016;54:445–56.
56. Hoffmeyer S, Burk O, von Richter O, Arnold HP, Brockmöller J, Johne A, et al. Functional polymorphisms of the human multidrug resistance gene: multiple sequence variations and correlation of one allele with P-glycoprotein expression and activity in vivo. Proc Natl Acad Sci USA. 2000;97:3473–8.
57. Takano A, Kusuhara H, Suhara T, Ieiri I, Morimoto T, Lee Y-J, et al. Evaluation of in vivo P-glycoprotein function at the blood–brain barrier among MDR1 gene polymorphisms by using ^{11}C-verapamil. J Nucl Med. 2006;47:1427–33.
58. Brunner M, Langer O, Sunder-Plassmann R, Dobrozemsky G, Müller U, Wadsak W, et al. Influence of functional haplotypes in the drug transporter gene ABCB1 on central nervous system drug distribution in humans. Clin Pharmacol Ther. 2005;78:182–90.
59. Mossel P, García-Varela L, Arif WM, van der Weijdan CWJ, Boersma HH, Willemsen ATM, et al. Evaluation of P-glycoprotein function at the blood–brain barrier using [^{18}F]MC225 PET. Eur J Nucl Med Mol Imaging. 2021. https://doi.org/10.1007/s00259-021-05419-8.
60. García-Varela L, Rodríguez-Pérez M, Custoida A, Moraga-Amaro R, Colabufo NA, Aguiar P, et al. In vivo induction of P-glycoprotein function can be measured with [^{18}F]MC225 and PET. Mol Pharm. 2021. https://doi.org/10.1021/acs.molpharmaceut.1c00302.